Direct comparison of three-terminal and four-terminal Hanle effects in the persistent photoconductor $Al_{0.3}Ga_{0.7}As$:Si

Joon-Il Kim [1,*], Tianhan Liu [1,*], Konstantinos Kountouriotis [1], Jun Lu,[2] Xuezhe Yu,[2] Yuwaraj Adhikari [1], Stephan von Molnár,[1] Jianhua Zhao,[2,†] and Peng Xiong [1,‡]

[1]*Department of Physics, Florida State University, Tallahassee, Florida 32306, USA*
[2]*State Key Laboratory of Superlattices and Microstructures, Institute of Semiconductors,*
Chinese Academy of Sciences, Beijing 100083, China

The electronic rendition of the Hanle effect, which is interpreted as the ensemble dephasing of a spin accumulation in the semiconductor under a perpendicular magnetic field, has been one of the most widely utilized and effective methods of measuring spin lifetime, spin accumulation, and spin transport in semiconductors. However, the origin of the Hanle magnetoresistance in the three-terminal (3T) setup has been intensively questioned both theoretically and experimentally; this is in contrast to the nonlocal four-terminal (NL-4T) measurement, which is accepted as reflecting spin accumulation and its spatial decay in metals and semiconductors alike. Here, we present results from 3T and NL-4T Hanle measurements on the *same* spin injection and detection devices with an $Al_{0.3}Ga_{0.7}As$:Si semiconducting channel. The use of $Al_{0.3}Ga_{0.7}As$:Si, a persistent photoconductor, enables examination of the evolution of both types of Hanle signals with varying carrier density in the channel on *one and the same* device via *in situ* photodoping. We observe that the 3T and NL-4T Hanle signals exhibit similar Lorentzian line shapes, and thus yield similar spin lifetimes at all carrier densities. Moreover, the amplitudes of both types of Hanle signals are found to be consistent with each other, showing a similar exponential decrease with carrier density and in agreement with the Valet-Fert theory, in contrast to devices with artificial oxide barriers. These observations provide compelling evidence that in devices in which the spin injectors and detectors are engineered to minimize the presence of localized states, the 3T Hanle measurements provide a reliable probe of the spin accumulation and its dynamics in the semiconductor channel.

I. INTRODUCTION

The efficient conversion of spin accumulation generated in a nonmagnetic semiconductor to an electrical signal is a necessary component of semiconductor spintronics. It is also of fundamental interest as a means for studying the spin dynamics and coherent spin transport in realistic device structures such as spin transistors and spin diodes [1,2]. The electrical signal conversion is often realized by contacting the semiconductor (SC) with a ferromagnetic (FM) electrode: The spin accumulation (spin splitting of the chemical potential) in the semiconductor and the spin polarization (spin-dependent electronic density of states at the chemical potential) in the ferromagnet result in an open-circuit voltage across the junction. The experimental implementation of the spin detection typically takes forms of a lateral spin valve or Hanle effect [3–5].

In the electronic rendition of the optical Hanle effect [6], a perpendicular magnetic field drives a precession of the polarized spins, and the associated dephasing leads to a decrease of the voltage. The decrease and eventual disappearance of the voltage with increasing field results in a Hanle curve of Lorentzian line shape [7]: The height of the curve is the magnitude of the spin accumulation, and the full width at half maximum (FWHM) yields the spin lifetime (τ_s). The Hanle effect has been one of the most widely utilized and effective methods of measuring spin lifetime, spin accumulation, and spin transport in SCs. It was first implemented in the nonlocal four-terminal (NL-4T) geometry [4,5], and the analysis based on a one-dimensional (1D) spin drift-diffusion (SDD) model provided rigorous proof that the measurements reflect spin accumulation and its temporal and spatial decays in the SC [4]. Later, a much simplified three-terminal (3T) geometry was applied on doped Si [8]. In the 3T setup, the spins injected into the SC from a ferromagnetic metal (FM) electrode are detected locally via Hanle measurement using the *same* FM electrode. The ease of device fabrication and measurement quickly made the 3T Hanle a popular method of spin detection on a variety of SCs [9]. However, the origin of the Hanle-like magnetoresistance (MR) in the 3T devices was later questioned intensively, due to a number of notable inconsistencies with an established theoretical model [10–12] and among the experimental results [7,13–18].

An outstanding issue in the 3T Hanle measurement is the apparent lack of definitive correlation between the widths of the experimental Hanle curves and the expected spin lifetimes in the SCs. This is reflected in a number of observations:

―――――――
*These authors contributed equally to this work.
†jhzhao@semi.ac.cn
‡pxiong@fsu.edu

The τ_s inferred from the 3T Hanle curves could vary by several orders of magnitude on the same SC materials with different oxide barriers [13] and ferromagnetic electrodes [7]. Conversely, τ_s from 3T devices with the same oxide barrier and ferromagnet showed no systematic variations with the spin-orbit interaction strength or doping level in the SCs [15]. Furthermore, in many cases, 3T Hanle measurements yielded τ_s which are 2–3 orders of magnitude smaller than the values inferred from NL-4T on the same devices [13,19]. In general, the large majority of the 3T Hanle experiments resulted in spin lifetimes that were 1–3 orders of magnitude smaller than theoretical predictions [20] and results of electron spin resonance [9,21,22] and NL-4T measurements [13,23–25]. Another important open question in the 3T Hanle experiments is the signal amplitudes. Again, in the majority of the experiments, the 3T Hanle amplitudes were observed to greatly exceed the expected values based on the Valet-Fert theory [26] and NL-4T measurements [13,24,25,27,28]. A particularly puzzling observation was a power-law dependence of the 3T Hanle amplitude on the specific junction resistance [the resistance-area (RA) product] [14,16], which is contrary to the expectation that the spin accumulation should be independent of the barrier resistance [10–12]. To account for the surprising sensitivity of the 3T Hanle amplitude to the tunnel barrier, several alternative scenarios were proposed [22,26,29,30]. To explain the unusually large 3T Hanle signals observed in Co/AlO$_x$/n-GaAs devices, Tran *et al.* [26] conjectured that spin accumulation occurs predominantly in the localized states in the oxide barrier instead of the SC channel; the much lower density of the localized states in the AlO$_x$, in comparison to the electronic density of states in the n-GaAs, produces a much larger spin splitting of the chemical potential. Jansen *et al.* [22] generalized the model by considering parallel conduction of hopping through the localized states as well as direct tunneling across the barrier, and the latter produces a finite spin accumulation in the SC independent of the barrier. Nevertheless, neither of the models could account for the experiments in which 3T Hanle measurements were performed in devices where the FM electrode was replaced by a nonmagnetic metal (Al) electrode [29,31,32]. The observation of Hanle-like MR curves in these devices pointed to an origin independent of any spin accumulation in the SC. A mechanism based on magnetic field modulation of the spin blockade of hopping electrons in the localized states was proposed [30,32], which was shown to account for all aspects of the 3T Hanle experiments in both the magnetic and nonmagnetic devices.

A ubiquitous feature of the 3T Hanle devices which showed these anomalous properties is an artificial oxide tunnel barrier between the FM electrode and the SC [9]. The tunnel barrier was necessary for overcoming the conductivity mismatch and achieving efficient spin injection [11,33,34]. A common alternative approach of engineering a tunnel barrier is via a thin Schottky barrier (SB). Epitaxial growth of Schottky junctions with a nanoscale graded doping profile was shown to be highly effective in enabling efficient spin injection [3,35]. In this work, we performed 3T and NL-4T Hanle measurements on the same spin-injection and detection devices with an Al$_{0.3}$Ga$_{0.7}$As:Si semiconducting channel, epitaxial Fe injector/detector, and graded SB in

between. Si-doped Al$_{0.3}$Ga$_{0.7}$As is a prototypical persistent photoconductor; its carrier density can be tuned via subband photoexcitation and the photoexcited carriers persist after the termination of illumination at low temperatures [36,37]. The persistent photoconductivity facilitates examination and direct comparison of the two types of Hanle signals on the *same* device over a large range of carrier densities across the insulator-to-metal transition (IMT) via *in situ* photodoping. In our devices, the 3T Hanle signals exhibit broad similarities with the NL-4T results in all aspects. The 3T and NL-4T Hanle curves have similar Lorentzian line shapes, and thus yield similar spin lifetimes at all carrier densities. Moreover, in contrast to devices with artificial oxide barriers, the amplitudes of the 3T Hanle signals show no anomalous enhancement, but rather are found to be consistent with those of NL-4T measurements and in agreement with the Valet-Fert theory [10–12]. The amplitudes of the 3T and NL-4T signals both show a similar exponential decrease with carrier density. These observations provide compelling evidence that in devices in which the spin injectors and detectors are engineered to minimize the presence of localized states, the 3T Hanle measurements are manifest of spin accumulation and dephasing, and provide a viable probe of the spin accumulation and its dynamics in the semiconductor channel.

II. EXPERIMENTS AND RESULTS

The overall experimental setup and methods, including the heterostructure and its growth, the device structure and fabrication procedure, the protocols employed for sample cooling and incremental *in situ* photodoping of the Al$_{0.3}$Ga$_{0.7}$As:Si channel, and the electrical characterizations of the devices with photodoping, are similar to what were described in previous reports [38,39]. The specific device structure and setup are shown in Fig. 1. Figure 1(a) is a schematic of the heterostructure used in this work, which was grown by molecular-beam epitaxy. Figure 1(b) is an optical micrograph of a fabricated device showing the overall structure, and Fig. 1(c) is a close-up image of the central region indicated by the dashed rectangle in Fig. 1(b). This is the device on which most of the data presented here were obtained. The three Fe electrodes have widths of (right to left) 5, 3, and 10 μm, with center-to-center distances of 6 and 8.5 μm. They were designed with different widths in the hope that the shape anisotropy would result in different coercive fields. However, we failed to obtain spin-valve signals with adequate consistency and predictability because of the dominant crystalline anisotropy in the epitaxial Fe electrodes. The device was mounted on a socket with an infrared light-emitting diode (LED) on top for photoillumination, as shown in Fig. 1(d). Devices were made and tested from six Fe/GaAs (AlGaAs) wafers with somewhat different structures and growth parameters. One wafer was identified on which three samples were fabricated, and they showed similar results in transport measurements. One sample was then chosen for full set of measurements. The sample reported in this paper was measured in three separate cooldowns, each time including a cooldown from room temperature and transport
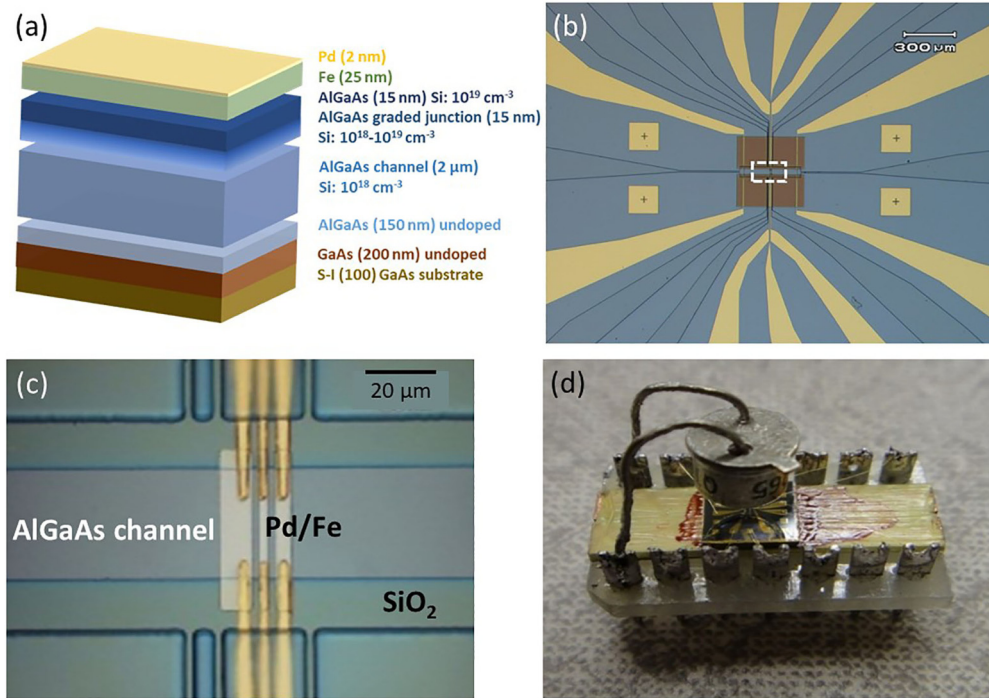
FIG. 1. (a) Schematic diagram of the heterostructure used for the spin devices in this work. (b) An optical image of a completed device. (c) Close-up optical image of the active region of the device in the dashed region in (b). (d) The photograph of a mounted sample on socket with an infrared LED for illumination.

measurements at low temperatures with different illuminations, showing consistent results. The data presented here are from one of the cooldowns with the most complete set of measurements.

The spin transport channel of the Si-doped $Al_{0.3}Ga_{0.7}As$ was designed to include Hall leads so that the carrier density and mobility of the channel could be determined simultaneously with the Hanle measurements on the same device at varying levels of photodoping. Figures 2(a) and 2(b) show resistivity and carrier density along with mobility, respectively, of the channel as functions of the cumulative illumination time, which span large ranges across the IMT. The critical carrier density for the IMT (n_c), indicated by the dashed line in Fig. 2(b), was determined with a protocol described in Ref. [37] to be 9.0×10^{16} cm^{-3}. Concomitant with the increase of the itinerant electron density in the $Al_{0.3}Ga_{0.7}As$, the resistance of an Fe/$Al_{0.3}Ga_{0.7}As$ junction on the device decreases and the current-voltage (I-V) characteristics evolve from rectifying to symmetric of decreasing nonlinearity, as shown in Fig. 2(c). The observations are consistent with a Schottky junction of decreasing width with photodoping of the $Al_{0.3}Ga_{0.7}As$.

Figure 3(a) illustrates the setups for 3T and NL-4T Hanle measurements. Prior to the Hanle measurements at each photodoping level, the Fe electrodes were first magnetized by a large in-plane magnetic field (~ 2 T). The red arrows indicate the magnetization direction of Fe electrodes. The sample holder was then rotated to the perpendicular configuration for Hanle measurements. All measurements were performed in a He^4 cryostat, mostly at 5 K. Figures 3(b) and 3(c) show a representative 3T and NL-4T Hanle signal, respectively, obtained at a bias current of 100 μA and carrier density

of 12.5×10^{16} cm^{-3}. The raw data and the process for the extraction of the Hanle signals were demonstrated in Supplemental Material 1 [40], including Ref. [3]. The resulting Hanle signals can then be fitted to the Lorentzian function or analyzed using the 1D SDD model [3]. In our devices, although the widths and separations of the Fe electrodes were comparable to the spin-diffusion lengths, all the Hanle curves were found to be well described by the Lorentzian function, similar to the case in short spin transport channels [41]. Following this protocol, we have obtained a comprehensive set of 3T and NL-4T Hanle data from the *same* device spanning a large parameter space of carrier densities and bias currents.

Figures 4(a) and 4(b) show the 3T (ΔV_{3T}) and NL-4T (ΔV_{4T1}) Hanle curves, respectively, at different carrier densities measured at a current of 200 μA. While the amplitudes of the NL-4T Hanle signals are about an order of magnitude smaller than the corresponding 3T Hanle signals (discussed later), it is apparent that the two types of Hanle curves share broad similarities in many respects: They have similar line shapes, and their FWHMs and amplitudes show similar dependences on the carrier density. In Figs. 4(c) and 4(d), the 3T and NL-4T Hanle amplitudes, respectively, are plotted against the carrier density for a range of different bias currents. For the NL-4T Hanle signals, it is apparent that in the low-density region (up to 35.6×10^{16} cm^{-3}), the amplitude decreases exponentially with increasing carrier density. At higher densities, the amplitudes of the measurable signals (with high bias currents) appear to deviate from the exponential decreases and plateau. For the 3T Hanle signals, at low carrier densities on the insulating side, the amplitudes decrease exponentially with n, albeit more gradually than the corresponding NL-4T
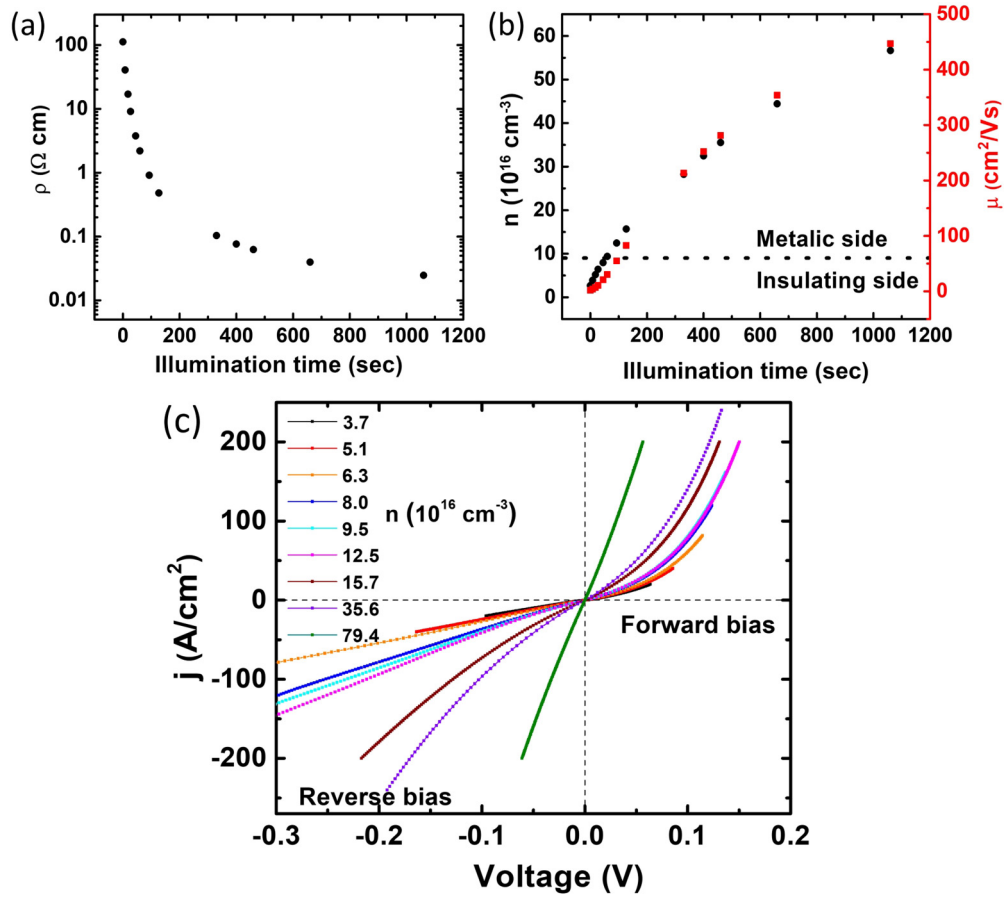
FIG. 2. (a) The resistivity and (b) carrier density and mobility of the $Al_{0.3}Ga_{0.7}As{:}Si$ channel vs the cumulative time of photoillumination. (c) The *j-V* characteristics for an Fe/AlGaAs junction at different carrier densities measured at 5 K in the 3T configuration.
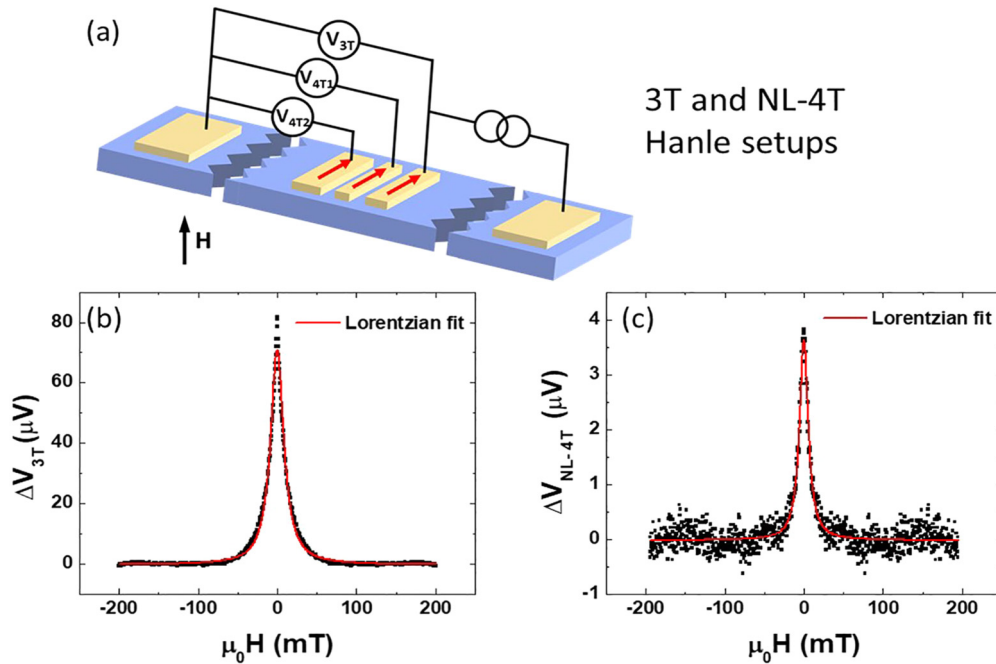

FIG. 3. (a) Schematics of the 3T and NL-4T Hanle measurement setups. The red arrows indicate the direction of the magnetization. A small perpendicular magnetic field is applied during the Hanle measurements. (b) and (c) show the 3T and NL-4T Hanle signals, respectively, after subtraction of the background (black) and the respective Lorentzian fit (red).
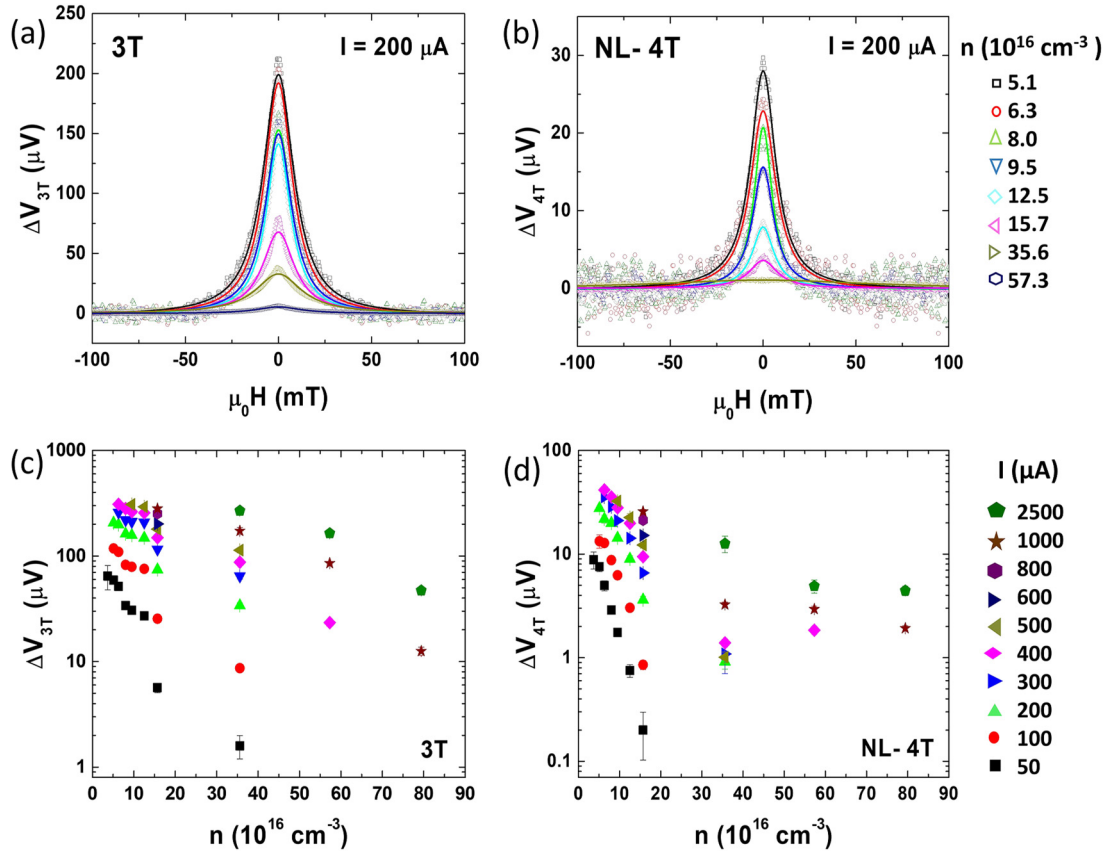
FIG. 4. Carrier density dependences of the Hanle signals. (a) 3T Hanle and (b) NL-4T Hanle signals at different carrier densities at a bias current of 200 μA. (c) 3T Hanle and (d) 4T Hanle signal amplitudes as functions of carrier density for different bias currents.

amplitudes (Supplemental Material 2 [40]). We believe that the exponential dependence of the Hanle amplitude with n originates primarily from the n dependence of r_N or ρ, which are nearly exponential at low carrier densities (Supplemental Material 3 [40]). Moreover, for each bias current, there is an abrupt drop of the amplitude across the IMT, as is evident in in Fig. 4(c), which is likely an experimental artifact.

Figures 5(a) and 5(b) show a set of 3T and NL-4T Hanle curves, respectively, at different bias currents for carrier density $n = 9.5 \times 10^{16}$ cm^{-3}, which is near the critical n for the IMT. Again, the overall line shapes for the two types of Hanle signals bear close resemblance, and their FWHMs and amplitudes show similar dependences on the carrier density. The variations of the amplitudes of the two types of Hanle signals at different carrier densities from insulating to metallic state are shown in Figs. 5(c) and 5(d).

III. DISCUSSION

A. Spin lifetime

The spin lifetimes can be determined from the Hanle measurements, using the FWHM of the Lorentzian function or fitting to the 1D SDD model. Details of the two types of analyses are presented in Supplemental Material 4 [40], including Ref. [8]. Figure 6(a) shows a comparison of the spin lifetimes extracted from the Lorentzian fit and SDD model analysis of the same set of 3T Hale measurements for various carrier densities, as well as the results from the

Lorentzian fit of simultaneous NL-4T Hanle measurements. Notably, the Lorentzian and 1D SDD analyses yield τ_s of similar magnitudes and carrier density dependences. The full set of spin lifetimes at varying carrier densities determined from the FWHMs of the 3T and NL-4T Hanle measurements on the same device is shown in Figs. 6(b) and 6(c), respectively. Although the absolute values of the spin lifetimes extracted from 3T and nonlocal 4T Hanle curves differ somewhat, they exhibit broadly similar variations with the carrier density: Both show little variation with the carrier density in the lower carrier density regime up to the vicinity of the IMT, beyond which the spin lifetime decreases with increasing carrier density. Deep into the metallic state, the spin lifetime reaches 1 ns or less; the steep decrease of τ_s with increasing n in the metallic state is qualitatively consistent with that observed in n-GaAs, which is attributed to enhanced Dyakonov-Perel spin relaxation [42]. However, both the τ_s obtained in this work and its decrease with n are more than an order of magnitude smaller than those from the electrical [3,4,43] and optical measurements [44] on n-GaAs on either side of the IMT. This is likely due to the much higher degree of disorder and momentum scattering in the AlGaAs alloy. Nevertheless, the fact that the 3T Hanle measurements yielded spin lifetimes consistent with the NL-4T Hanle and resolved the expected decrease of τ_s with increasing n provides strong evidence that the 3T Hanle effect in our devices is manifest of the spin dynamics in the SC channel.
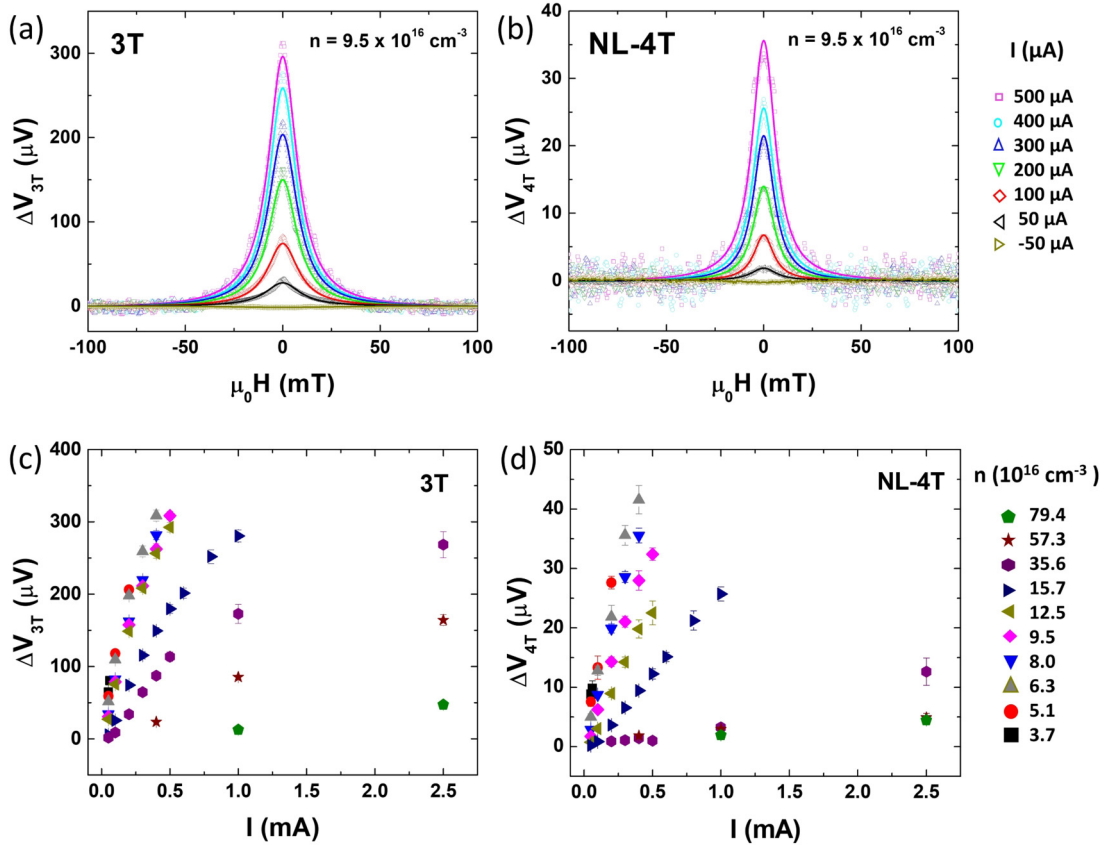
FIG. 5. The bias dependences of Hanle signals. (a) 3T Hanle and (c) 4T Hanle signals at different bias currents with the carrier density of 9.5×10^{16} cm^{-3}. The magnitude of (b) 3T Hanle and (d) 4T Hanle signals vs bias current at different carrier densities.

IV. 3T HANLE AMPLITUDE

A theoretical model of the Hanle effect formulated by Fert and coworkers [10–12] predicts a spin accumulation linear with the bias current:

$$\Delta V = \frac{\gamma}{e}(\Delta\mu)_I = \frac{\gamma r_N(\beta r_F + \gamma r_b^*)}{r_F + r_N + r_b^*} j, \qquad (1)$$

where $(\Delta\mu)_I$ is the spin accumulation in the semiconductor channel at the interface, γ is the spin-asymmetry coefficient of the interface resistance, and β is the bulk asymmetry coefficient. $r_F = \rho_F \lambda_{sf}^F$ and $r_N = \rho_N \lambda_{sf}^N$ are the spin resistivity, namely the product of resistivity and spin-diffusion length of the FM and SC, respectively. r_b^* is the specific resistivity of the interface between FM and SC, and j is the current density. As $r_F \ll r_N$ and r_b^*, Eq. (1) is reduced to

$$\Delta V \approx \frac{\gamma^2 r_N r_b^*}{r_N + r_b^*} j. \qquad (2)$$

In this equation, all the parameters are material dependent. Therefore, our experimental setup, with 3T Hanle, NL-4T Hanle, and the resistivity and carrier density of the SC measured on the same device under increasing *in situ* photodoping, offered a unique platform for a systematic and rigorous comparison with the theory. Note that the spin-asymmetry coefficient γ generally depends not only on the spin polarization of the FM but also on the nature of the FM/SC interface of the heterostructure.

In Fig. 7(a), we plot the spin resistance-area (spin-*RA*) product, $R_s A = \Delta V_{3T}(B_z = 0)/j$, at different bias currents for the device at various photodoping levels. The nonlinearity of the Hanle signals manifests as nonmonotonic variations of the spin-*RA* product with bias current. Figure 7(b) plots the spin-*RA* products versus carrier densities for various bias currents. In spite of the variations with bias currents originated from the nonlinearity, an exponential decrease of the spin-*RA* with increasing carrier density is apparent. Because γ was not independently measured in our experiments, a parameter-free comparison with the Valet-Fert model is not possible. We first calculate the spin-*RA* using the optimum value of $\gamma = 0.4$ [45] and the experimentally determined electron (*charge*) diffusion constants from measured resistivity and carrier density for a few photodoping levels in the vicinity of the IMT (Supplemental Material, Table S1 [40]). The resulting values are indicated by the solid lines in Fig. 7(a), which fall within the ranges of experimental results at carrier densities near the IMT or higher. This is notable in light of the varied and significant disagreement between theory and experiment in 3T Hanle devices with oxide barriers. However, the electron diffusion constants and spin lifetimes used in the calculations above correspond to spin-diffusion lengths which are unphysically short (see more discussion below), which essentially invalidates the assumption of a constant optimum γ. Alternatively, we use the spin-diffusion length inferred from Fig. 8 (which is approximately 3.5 μm for these carrier densities) and the maximum value of measured spin-*RA* for each carrier density
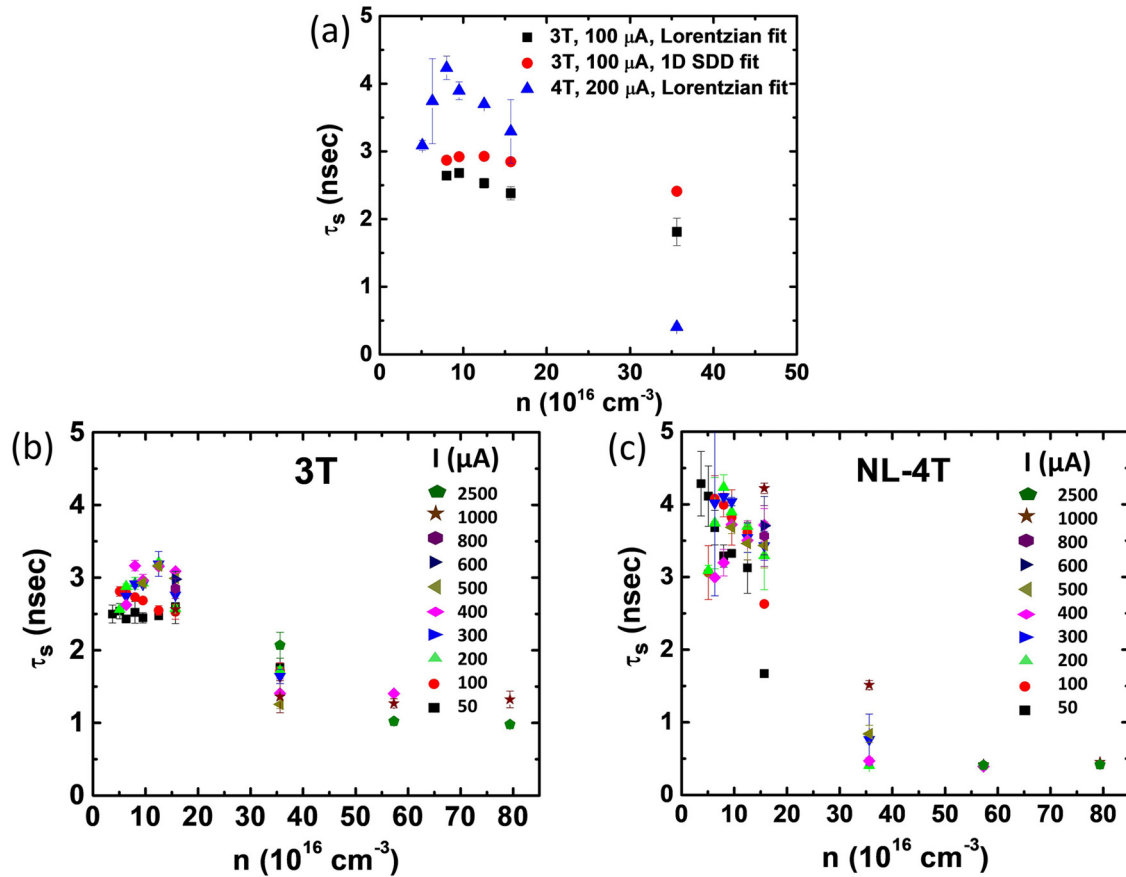
FIG. 6. (a) A comparison of spin lifetime τ_s extracted from Lorentzian fit and 1D SDD model analysis for the 3T and NL-4T Hanle measurements. Carrier density dependences of the spin lifetimes determined from (b) 3T and (c) NL-4T Hanle measurements at various bias currents.

[indicated by dashed lines in Fig. 7(a)] to calculate γ. The resulting γ increases with increasing carrier density, from 0.05 for $n = 9.5 \times 10^{16}\,\mathrm{cm}^{-3}$ to 0.16 for $n = 35.6 \times 10^{16}\,\mathrm{cm}^{-3}$.

The range of γ variation with n is physically plausible, making this the likely scenario. The relevant parameters can be found in Table S2 in the Supplemental Material [40].
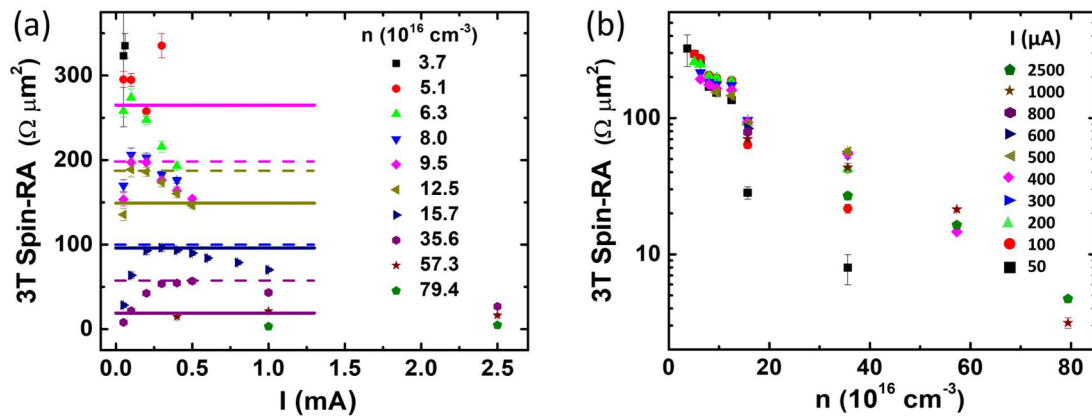

FIG. 7. Spin resistance-area products of the 3T Hanle effect plotted for (a) varying bias currents at various channel carrier densities, and (b) varying channel carrier densities at various bias currents. The solid lines in (a) represent the theoretical values expected from the Valet-Fert model [10–12] with $\gamma = 0.4$ based on experimentally determined charge diffusion constants and spin lifetimes. The dashed lines in (a) indicate the maximum values of the measured spin-RA, which were used to calculate γ based on the spin-diffusion length inferred from Fig. 8 ($\sim$3–4 μm).
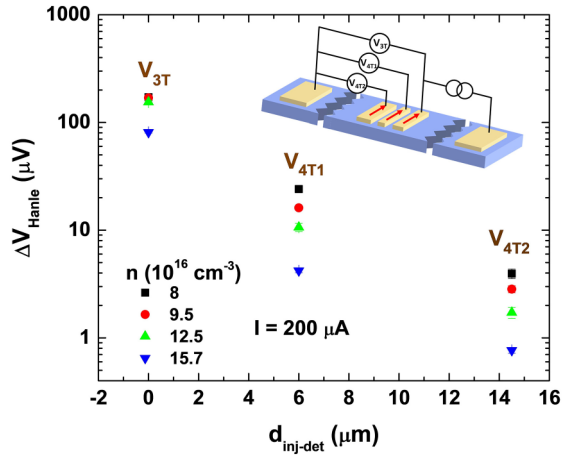
FIG. 8. Amplitudes of the 3T Hanle signals and NL-4T Hanle signals from two different detecting electrodes of different center-to-center injector-detector distances for different carrier densities. Inset: Schematic of the three configurations of Hanle measurements.

A. Comparison of 3T and NL-4T Hanle amplitudes

Our experimental setup facilitated a direct comparison of the 3T and NL-4T Hanle amplitudes using the same set of FM electrodes in the same device at varying carrier densities in the SC channel. Figure 8 shows the variations of the amplitude of the Hanle signal with the distance between the spin injector and detector at four different carrier densities. The Hanle measurements with three configurations shown in the inset of Fig. 8 share the same reference electrode. Two sets of Hanle curves ($n = 8 \times 10^{16}$ cm^{-3} and $n = 9.5 \times 10^{16}$ cm^{-3}) are presented in Supplemental Material 5 [40]. The 3T Hanle signals are consistent with the nonlocal 4T Hanle signals based on a simple exponential decay of spin accumulation; the 3T signal lies slightly above the extrapolation of the NL-4T Hanle signals, which may be attributed to the enhancement of the spin signal detected under bias [46] discussed earlier. In the 3T Hanle setup, the same electrode serves as the injector and detector, and the distance is set to be zero. Although the NL-4T Hanle signals were limited to only two different injector-detector distances, the exponential fits to the three points yield λ_s between 3 to 4 μm for the four carrier densities. More important to the topic discussed here, the results in Fig. 8 are direct demonstration of the consistency of the 3T and NL-4T Hanle measurements in our devices.

Finally, as alluded to earlier, the spin-diffusion length can also be calculated from the experimentally determined spin lifetime and electron (*charge*) diffusion constant, which, however, yield unphysically short spin-diffusion lengths of

0.03–0.14 μm. A possible origin for this discrepancy is that the charge and spin-diffusion constants could be significantly different for several reasons [47–51], particularly at low temperatures and high carrier densities [48]. Also, the diffusivities of the majority spins and minority spins could be different, as suggested by Flatté and coworkers [47,49].

V. CONCLUSIONS

In this work, the 3T and nonlocal 4T Hanle measurements were measured simultaneously on the same device. Moreover, utilizing the persistent photoconductivity in the AlGaAs, the 3T and nonlocal 4T Hanle signals were compared directly over a broad range of carrier densities. The magnitudes of the 3T and nonlocal 4T Hanle curves both show exponential decay with increasing channel carrier density. Also, the bias current dependencies of the 3T and nonlocal 4T Hanle signal magnitudes bear close resemblance for a number of carrier densities.

Spin lifetimes have been obtained by fitting the 3T and nonlocal 4T Hanle data to both the Lorentzian function and 1D SDD model. In both cases, the spin lifetimes extracted from 3T Hanle curves are comparable to those from the nonlocal 4T Hanle curves, and they exhibit similar variation with photodoping. The spin lifetimes from the Lorentzian fits are consistently lower than the values from the 1D SDD analysis, which reflects the known fact that the Lorentzian fit a lower bound of the spin lifetimes.

The consistency between the 3T Hanle and nonlocal 4T measurements was further evidenced by the exponential correlation between their magnitudes: The 3T signal measured at the spin injector and nonlocal 4T signals measured at two different spin detectors yield results consistent with an exponential decay of the spin accumulation with the transport distance. Based on the broad similarities and consistency between the 3T and nonlocal 4T Hanle measurements in our devices, we conclude that in heterostructures with epitaxial Schottky junctions as spin injectors and detectors, the 3T Hanle signals indeed reflect spin accumulation in the semiconductor channel.

[1] S. Datta and B. Das, Appl. Phys. Lett. **56**, 665 (1990).

[2] I. Žutić, J. Fabian, and S. Das Sarma, Rev. Mod. Phys. **76**, 323 (2004).

[3] X. Lou, C. Adelmann, M. Furis, S. A. Crooker, C. J. Palmstrøm, and P. A. Crowell, Phys. Rev. Lett. **96**, 176603 (2006).

[4] X. Lou, C. Adelmann, S. A. Crooker, E. S. Garlid, J. Zhang, K. S. M. Reddy, S. D. Flexner, C. J. Palmstrøm, and P. A. Crowell, Nat. Phys. **3**, 197 (2007).

[5] O. M. J. van 't Erve, A. T. Hanbicki, M. Holub, C. H. Li, C. Awo-Affouda, P. E. Thompson, and B. T. Jonker, Appl. Phys. Lett. **91**, 212109 (2007).

[6] W. Hanle, Z. Phys. D: Atoms, Mol. Clust. **18**, 5 (1991).

[7] S. P. Dash, S. Sharma, J. C. Le Breton, J. Peiro, H. Jaffrès, J.-M. George, A. Lemaître, and R. Jansen, Phys. Rev. B **84**, 054410 (2011).

[8] S. P. Dash, S. Sharma, R. S. Patel, M. P. de Jong, and R. Jansen, Nature (London) **462**, 491 (2009).

[9] O. Txoperena and F. Casanova, J. Phys. D: Appl. Phys. **49**, 133001 (2016).

[10] T. Valet and A. Fert, Phys. Rev. B **48**, 7099 (1993).

[11] A. Fert and H. Jaffrès, Phys. Rev. B **64**, 184420 (2001).

[12] A. Fert, J.-M. George, H. Jaffres, and R. Mattana, IEEE Trans. Electron Devices **54**, 921 (2007).

[13] Y. Aoki, M. Kameno, Y. Ando, E. Shikoh, Y. Suzuki, T. Shinjo, M. Shiraishi, T. Sasaki, T. Oikawa, and T. Suzuki, Phys. Rev. B **86**, 081201(R) (2012).

[14] T. Uemura, K. Kondo, J. Fujisawa, K. Matsuda, and M. Yamamoto, Appl. Phys. Lett. **101**, 132411 (2012).

[15] A. Dankert, R. S. Dulal, and S. P. Dash, Sci. Rep. **3**, 3196 (2013).

[16] S. Sharma, A. Spiesser, S. P. Dash, S. Iba, S. Watanabe, B. J. van Wees, H. Saito, S. Yuasa, and R. Jansen, Phys. Rev. B **89**, 075301 (2014).

[17] H. N. Tinkey, P. Li, and I. Appelbaum, Appl. Phys. Lett. **104**, 232410 (2014).

[18] A. G. Swartz, S. Harashima, Y. Xie, D. Lu, B. Kim, C. Bell, Y. Hikita, and H. Y. Hwang, Appl. Phys. Lett. **105**, 032406 (2014).

[19] L.-T. Chang, W. Han, Y. Zhou, J. Tang, I. A. Fischer, M. Oehme, J. Schulze, R. K. Kawakami, and K. L. Wang, Semicond. Sci. Technol. **28**, 015018 (2013).

[20] Y. Song, O. Chalaev, and H. Dery, Phys. Rev. Lett. **113**, 167201 (2014).

[21] V. Zarifis and T. G. Castner, Phys. Rev. B **57**, 14600 (1998).

[22] R. Jansen, A. M. Deac, H. Saito, and S. Yuasa, Phys. Rev. B **85**, 134420 (2012).

[23] C. H. Li, O. M. J. van 't Erve, and B. T. Jonker, Nat. Commun. **2**, 245 (2011).

[24] Y. Zhou, W. Han, L.-T. Chang, F. Xiu, M. Wang, M. Oehme, I. A. Fischer, J. Schulze, R. K. Kawakami, and K. L. Wang, Phys. Rev. B **84**, 125323 (2011).

[25] T. Suzuki, T. Sasaki, T. Oikawa, M. Shiraishi, Y. Suzuki, and K. Noguchi, Appl. Phys. Express **4**, 023003 (2011).

[26] M. Tran, H. Jaffrès, C. Deranlot, J.-M. George, A. Fert, A. Miard, and A. Lemaître, Phys. Rev. Lett. **102**, 036601 (2009).

[27] T. Sasaki, T. Suzuki, Y. Ando, H. Koike, T. Oikawa, Y. Suzuki, and M. Shiraishi, Appl. Phys. Lett. **104**, 052404 (2014).

[28] J. Shiogai, M. Ciorga, M. Utz, D. Schuh, M. Kohda, D. Bougeard, T. Nojima, J. Nitta, and D. Weiss, Phys. Rev. B **89**, 081307 (2014).

[29] O. Txoperena, Y. Song, L. Qing, M. Gobbi, L. E. Hueso, H. Dery, and F. Casanova, Phys. Rev. Lett. **113**, 146601 (2014).

[30] Y. Song and H. Dery, Phys. Rev. Lett. **113**, 047205 (2014).

[31] O. Txoperena, M. Gobbi, A. Bedoya-Pinto, F. Golmar, X. Sun, L. E. Hueso, and F. Casanova, Appl. Phys. Lett. **102**, 192406 (2013).

[32] H. Inoue, A. G. Swartz, N. J. Harmon, T. Tachikawa, Y. Hikita, M. E. Flatté, and H. Y. Hwang, Phys. Rev. X **5**, 041023 (2015).

[33] E. I. Rashba, Phys. Rev. B **62**, R16267 (2000).

[34] G. Schmidt, D. Ferrand, L. W. Molenkamp, A. T. Filip, and B. J. van Wees, Phys. Rev. B **62**, R4790 (2000).

[35] B. T. Jonker, G. Kioseoglou, A. T. Hanbicki, C. H. Li, and P. E. Thompson, Nat. Phys. **3**, 542 (2007).

[36] S. Katsumoto, F. Komori, N. Sano, and S. Kobayashi, J. Phys. Soc. Jpn. **56**, 2259 (1987).

[37] J. Misuraca, J. Trbovic, J. Lu, J. Zhao, Y. Ohno, H. Ohno, P. Xiong, and S. von Molnár, Phys. Rev. B **82**, 125202 (2010).

[38] J. Misuraca, J.-I. Kim, J. Lu, K. Meng, L. Chen, X. Yu, J. Zhao, P. Xiong, and S. von Molnár, Appl. Phys. Lett. **102**, 152408 (2013).

[39] J. Misuraca, J.-I. Kim, J. Lu, K. Meng, L. Chen, X. Yu, J. Zhao, P. Xiong, and S. von Molnár, Appl. Phys. Lett. **104**, 082405 (2014).

[40] See Supplemental Material at http://link.aps.org/supplemental/10.1103/PhysRevMaterials.6.024603 for analysis of Hanle signals, the carrier density dependence of Hanle signals, spin resistance, junction-specific resistance, and channel resistivity, comparison of spin lifetimes from fittings to Lorentzian function and 1D SDD model, Hanle curves in 3T and 4T configurations, device parameters under different illumination time, calculated spin-RA and spin-asymmetry coefficient γ, including Refs. [3,8].

[41] M. Gurram, S. Omar, and B. J. van Wees, Nat. Commun. **8**, 248 (2017).

[42] S. A. Crooker, E. S. Garlid, A. N. Chantis, D. L. Smith, K. S. M. M. Reddy, Q. O. Hu, T. Kondo, C. J. Palmstrøm, and P. A. Crowell, Phys. Rev. B **80**, 041305(R) (2009).

[43] M. D'Yakonov and V. Perel', Sov. Phys.-JETP **38**, 177 (1974).

[44] M. Furis, D. L. Smith, S. A. Crooker, and J. L. Reno, Appl. Phys. Lett. **89**, 102102 (2006).

[45] R. I. Dzhioev, K. V. Kavokin, V. L. Korenev, M. V. Lazarev, B. Y. Meltser, M. N. Stepanova, B. P. Zakharchenya, D. Gammon, and D. S. Katzer, Phys. Rev. B **66**, 245204 (2002).

[46] T. J. Zega, A. T. Hanbicki, S. C. Erwin, I. Žutić, G. Kioseoglou, C. H. Li, B. T. Jonker, and R. M. Stroud, Phys. Rev. Lett. **96**, 196101 (2006).

[47] M. E. Flatté and J. M. Byers, Phys. Rev. Lett. **84**, 4220 (2000).

[48] I. D'Amico and G. Vignale, Europhys. Lett. **55**, 566 (2001).

[49] Z. G. Yu and M. E. Flatté, Phys. Rev. B **66**, 201202 (2002).

[50] C. P. Weber, N. Gedik, J. E. Moore, J. Orenstein, J. Stephens, and D. D. Awschalom, Nature (London) **437**, 1330 (2005).

[51] F. Cadiz, V. Notot, J. Filipovic, D. Paget, C. P. Weber, L. Martinelli, A. C. H. Rowe, and S. Arscott, J. Appl. Phys. **122**, 095703 (2017).